

Design and Implementation of a Uniplanar Gradient Field Coil for Magnetic Resonance Imaging

ROSTISLAV LEMDIASOV,¹ REINHOLD LUDWIG,¹ MAT BREVARD,² CRAIG FERRIS²

¹ Department of Electrical and Computer Engineering, Worcester Polytechnic Institute, Worcester, MA 01609

² Behavioral Neuroscience Program, Department of Psychiatry, 55 Lake Avenue North, University of Massachusetts Medical Center, Worcester, MA 01655

ABSTRACT: A new approach to design uniplanar gradient coils for magnetic resonance imaging (MRI) is presented. The theoretical formulation involves a constraint cost function between the desired field in a particular region of interest in space and the current-carrying coil plane based on Biot-Savart's integral equation. An appropriate weight function in conjunction with linear approximation functions allows the transformation of the problem formulation into a linear matrix equation in which its iterative solution yields discrete current elements in terms of magnitude and direction within the prescribed coil plane. These current elements can be synthesized into an overall practical wire configuration by suitably adding individual wire loops. Numerical predictions and practical testing for a G_y gradient coil underscore the success of this approach in terms of achieving a highly linear field while maintaining low parasitic fields. © 2004 Wiley Periodicals, Inc. Concepts Magn Reson Part B (Magn Reson Engineering) 20B: 17–29, 2004

KEY WORDS: uniplanar gradient coils; magnetic resonance; constraint optimization; localized uniform field gradient

INTRODUCTION

Magnetic resonance imaging (MRI) has been used as a powerful, noninvasive diagnostic tool in the anatomical and functional study of biological soft tissue. Its technology rests on the interaction of three different magnet systems: the main high-field magnet capable of producing field strengths in the several tesla range, the gradient coils needed to select a particular region of interest, and the radio frequency (RF) coil or resonator required to transmit and receive the MR signal response. Recently, the main magnet system

has received considerable interest because of the demand for increased flux densities beyond 2 T. Present superconducting magnets have already reached 7 T for humans (1) and 11.7 T (2) for animal studies. Similarly, RF coils have experienced major improvements since the birdcage (3) design was introduced in the mid-1980s. Current state-of-the-art technology involves resonator structures introduced by Vaughan et al. (4) and microstrip designs by Bogdanov and Ludwig (5) that have been applied for resonance frequency up to 500 MHz, corresponding to proton imaging at 11.74 T (6).

Comparatively little research has gone into gradient coils, even though it is well documented that poor field linearity or high parasitic fields can result in serious image distortion (7). Moreover, gradient coils with large inductances and/or resistances can negatively impact switching performance when driven by fast pulse sequences (8). For high-field animal re-

Received 22 May 2003; accepted 6 August 2003

Correspondence to: Reinhold Ludwig; E-mail: ludwig@wpi.edu

Concepts in Magnetic Resonance Part B (Magnetic Resonance Engineering), Vol. 20B(1) 17–29 (2004)

Published online in Wiley InterScience (www.interscience.wiley.com). DOI 10.1002/cmr.b.20003

© 2004 Wiley Periodicals, Inc.

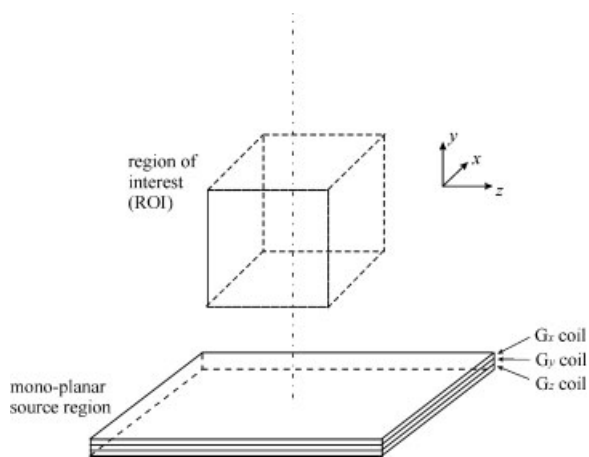


Figure 1 Conceptual arrangement of three monoplanar surface gradient coils situated below the ROI.

search, particularly as applied to functional imaging, the region of interest (ROI) typically is very narrowly focused to cranial regions not larger than $\sim 3\text{--}4\text{ cm}^3$ in small rodents such as rats and mice. For these applications large, encircling coil configurations are inefficient when compared with open, planar or biplanar configurations (9, 10). A number of theoretical design approaches have been devised that are based on either analytical or numerical optimization procedures. In particular, there are several analytical inverse formulations leading to (a) energy-minimal coil designs (11, 12), (b) inductance-minimal coil designs (13), and (c) designs that lead to best approximations of the desired field (14). In addition, hybrid designs have been proposed that combine these approaches by introducing each function to be minimized with its own weight (15). These variational approaches, based on Biot-Savart's integral formulations or classical series expansions, are computationally efficient to implement and generally yield acceptable results. Alternatively, numerical methods are more flexible in solving the forward problem, i.e., computing the field distribution because of a known current flow pattern. This is particularly true if complicated boundary conditions, heterogeneous media, and transient current excitations are affected (16). However, when combining the numerical modeling strategy with optimization techniques like complex method, steepest descent, and conjugate gradient, these methods often become prohibitively intensive.

In this article, a new method of solving for the current-carrying wire configuration of a uniplanar surface gradient coil is presented. The approach relies on formulating a constraint optimization procedure that establishes the planar current density for a desired field distribution in space. Although the current is

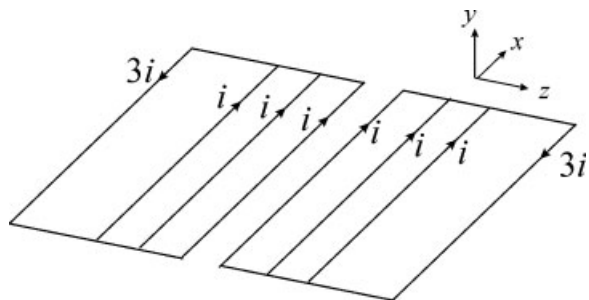


Figure 2 G_y gradient coil design as originally proposed by Cho and Yi (17).

found for discrete wire segments in terms of magnitude and direction, the actual coil realization is easy and straightforward to implement. It will be shown that this coil yields a better performance compared with the one described in the literature (17, 18).

DESIGN GOAL AND QUALITY ASSESSMENT

It is a well-established fact that linear and concomitantly strong magnetic gradient fields enable the high-resolution imaging of biological tissue. The goal of this research is to design an effective surface gradient coil (Fig. 1) in a prescribed, spatially very restrictive plane. Effectiveness in this context is understood as the ability to provide a high gradient magnetic field, while minimizing the parasitic gradient contributions within the region of interest (ROI).

For the subsequent theoretical and practical coil considerations, we need to define certain criteria that greatly facilitate the comparison of the various coil designs. In particular, three criteria are needed:

- *Gradient strength.* Obviously, the image resolution improves if the gradient coil is able to produce a higher field magnitude for the same amount of input current.
- *Field uniformity.* Distortions in the image are minimized if the magnetic field is highly linear in the ROI. As discussed later in this work, we can estimate the field uniformity visually from the magnetic field plots and from the image of the distorted phantom.
- *Parasitic gradient field distribution.* To assess the overall quality of the gradients (e.g., the G_y coil), a so-called coil quality factor Q can be defined as

$$Q = \min_{\text{ROI}} \left(\frac{|G_y|}{\sqrt{G_x^2 + G_y^2 + G_z^2}} \right)$$

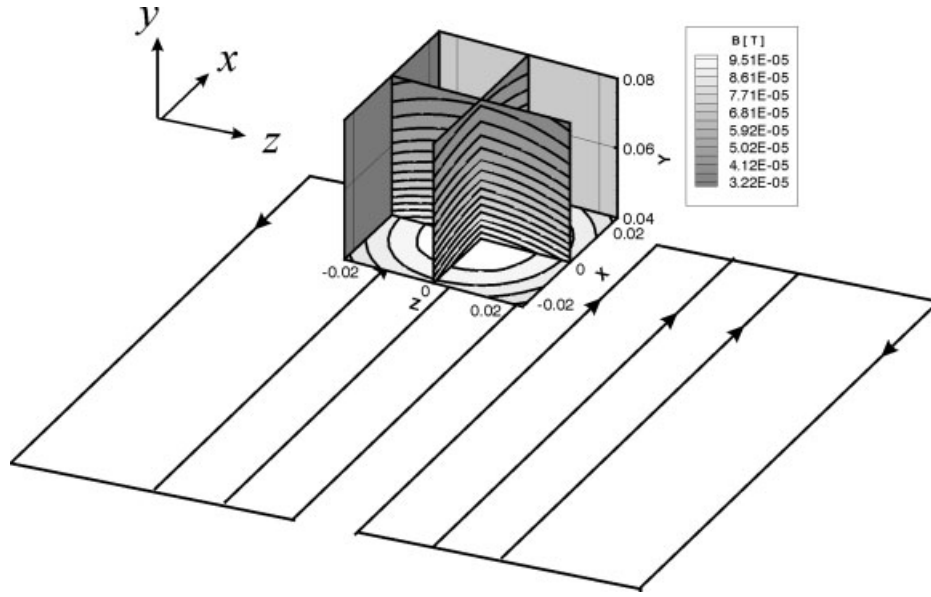


Figure 3 Magnetic flux density B_z in units of tesla for both the transversal and the longitudinal direction throughout the ROI. The ROI is located 4 cm above the coil plane and ranges from 4 to 8 cm in y -directions and from -2.5 to $+2.5$ cm in z - and x -directions, respectively.

The coil that maximizes Q is preferred in the sense that it yields the lowest parasitic gradients.

PRIOR ART

One of the key monoplanar surface gradient coil designs was reported by Cho and Yi (17). In their study, they described a three-channel set consisting of the X -, Y -, and Z -gradient coils as schematically depicted in Fig. 2 for the G_y surface coil. In Fig. 3, we have computed the z -component of the magnetic flux density based on Biot-Savart's law and for a normalized input current of $i = 1A$. We observe that the magnetic

field exhibits parasitic gradients in x - and z -directions. This is seen more clearly in Fig. 4, where we again show the transversal and longitudinal slices taken through the center of the ROI.

Because nonlinear field distributions result in image distortions, it is important to visualize the exact extent of the magnetic field behavior. As we observe from Fig. 4, points having the same magnetic field value are located on slightly curved contour lines (magnitude level of the magnetic field). The underlying MRI Fourier space reconstruction approach treats points that have the same field level as belonging to the same y -coordinate. In fact, those points of constant magnetic field values in Fig. 4 would become

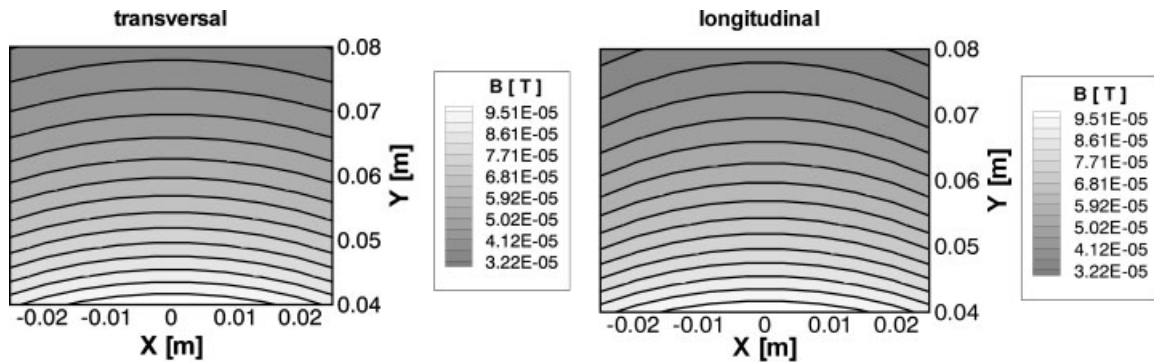


Figure 4 Contours of magnetic flux density in units of tesla in transversal and longitudinal cross-sections through the ROI. The spatial dimensions in x -, y -, and z -directions are given in meters.

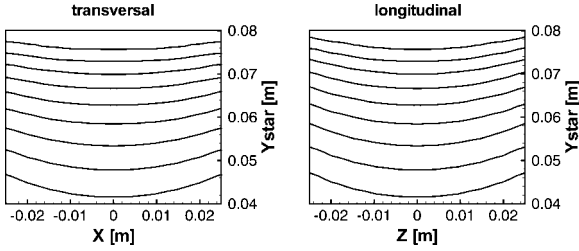


Figure 5 Simulations of the reconstructed image produces by the G_y gradient coil designed by Cho and Yi (17) with levels of y in terms of (z, x, y^*) coordinates. Here, y^* (or YSTAR) is the predicted y -coordinate after Fourier space reconstruction. All spatial dimensions are recorded in meters.

straight, equidistant lines after Fourier space reconstruction. To assess the degree of distortion, it is advantageous to plot the y -coordinate values within the ROI in a new $(z, x, \text{and } B_z)$ coordinate representation. In other words, we consider y as a function of x and B_z . Thus, we can associate values of B_z with a new coordinate y^* (the y -coordinate after Fourier space reconstruction) such that

$$y^* = 0.04 + \frac{0.08 - 0.04}{B_z(y = 0.08) - B_z(y = 0.04)} \times (B_z - B_z(y = 0.04)) \text{ [m]}$$

where y^* depends linearly on B_z . Indeed, we can now plot y in a $(z, x, \text{and } y^*)$ coordinate representation. Contours of constant y reveal the extent of how straight lines in the ROI are distorted after Fourier space reconstruction for a particular G_y coil design.

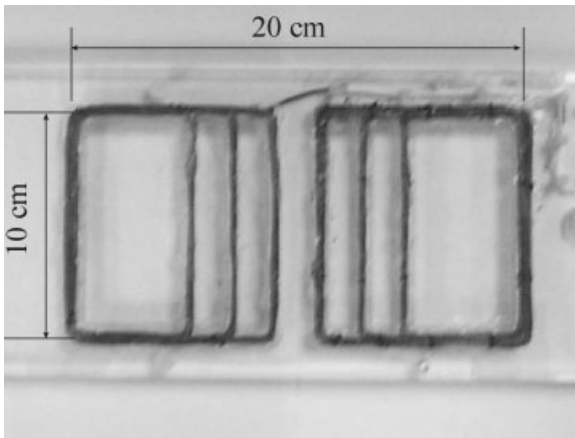


Figure 6 Fabrication of prior art G_y gradient coil (17). The particular wire arrangement forms the baseline for subsequent comparisons against our new improved coil designs.

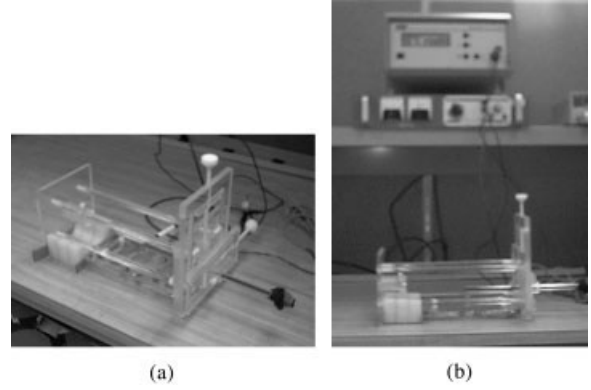


Figure 7 (a) G_y coil (17) in a Plexiglas restrainer; (b) experimental setup for bench testing.

As an example, the G_y coil designed by Cho (17) yields a simulated reconstruction image as shown in Fig. 5. As clearly seen in this figure, the space within the ROI closest to the coil appears to be significantly expanded and curved.

In addition, as a single figure of merit, we also can use the coil quality factor Q to assess the overall G_y performance. Applying Q for the coil designed by Cho (17), we obtain $Q = 0.867$. This coil was built by us for baseline purposes using a plastic former (of thickness 12 mm) and wiring of the American Wire Gauge (AWG) 20 copper wires. The wire pattern was wound around a suitably arranged template of metal pegs mounted on a wooden plate, before being transferred into a plastic former with milled groove. The wire pattern is spatially constrained within the grooves by using an epoxy resin. A photograph of the finished G_y coil is seen in Fig. 6.

This coil has an inductance and resistance of $L_s = 0.315$ mH and $R_s = 1.39 \Omega$, respectively. The actual coil was bench tested using a specially designed non-

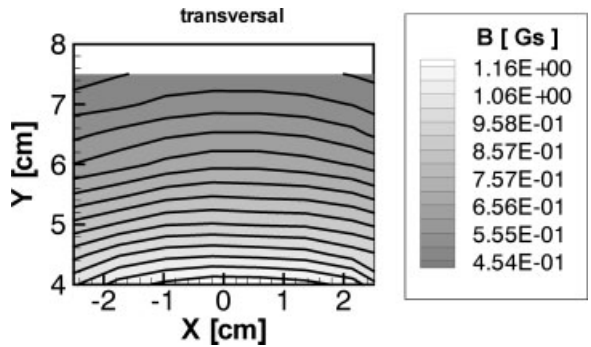


Figure 8 Measured transversal magnetic field B_z in gauss recorded for the G_y gradient coil as proposed in Ref. (17) and based on a drive current of 1 A. Spatial dimensions are recorded in centimeters.

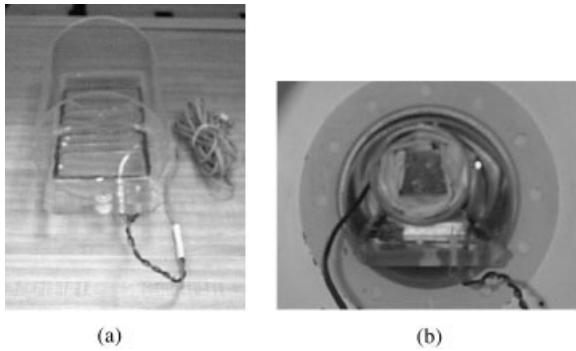


Figure 9 Original G_y coil (17): (a) on the bench, placed in a Plexiglas cylindrical tube 15 cm in diameter and (b) located inside the MR system.

magnetic plastic holder, as depicted in Fig. 7(a). Based on an applied direct current (DC) of 1 A, the magnetic field in the ROI was measured with a Hall sensor attached to a Gaussmeter [Fig. 7(b)]. The measured magnetic field of the coil in a transversal (or X - Y) plane was measured and plotted in Fig. 8.

The foregoing G_y coil arrangement was tested in a GE CSI-II 2.0 T 45-cm imaging spectrometer (General Electric, Schenectady, NY) operated at 85.56 MHz and residing within a commercial self-shielded gradient set. The constructed G_y coil was placed in the 5-mm-thick Plexiglas plastic tube (Plastics Unlimited, Worcester, MA) and fastened with plastic screws as shown in Fig. 9.

In addition to the G_y surface coil, a custom-built 12-element low-pass RF birdcage coil of 10 cm in diameter was fastened on the coil plane. Inside the RF coil a Plexiglas phantom 5.0 cm wide (transverse direction), 5.0 cm long (longitudinal direction), and 3.9 cm high was positioned as seen in Fig. 10. The phantom has six water-filled compartments, each 3 mm thick, and the compartments are separated by 3-mm-thick Plexiglas layers. Epoxy resin was used to provide reliable adhesion of the phantom layers.

After inserting the coil within the main magnet, which was equipped with a standard three-channel GE gradient set, the following steps were performed:

1. The gradient amplifier cable link leading to the GE G_y channel was disconnected and attached to the new G_y surface gradient coil.
2. The resistance ($R = 33.4 \text{ k}\Omega$) and capacitance ($C = 3.17 \text{ nF}$) values within the feedback control loop at the output stage of the G_y gradient amplifier were adjusted so as to compensate for the induced eddy current influence. The numerical values were selected such that an applied rectangular pulse sent to the G_y surface

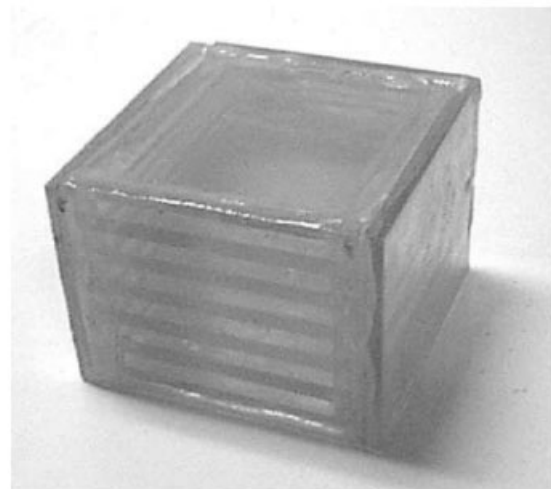
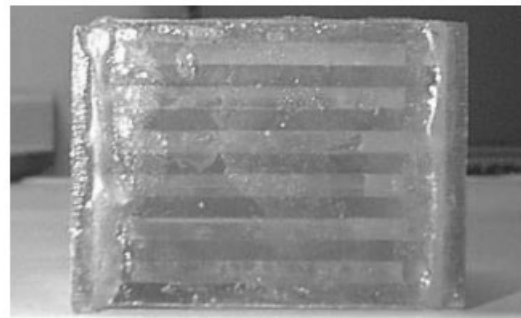
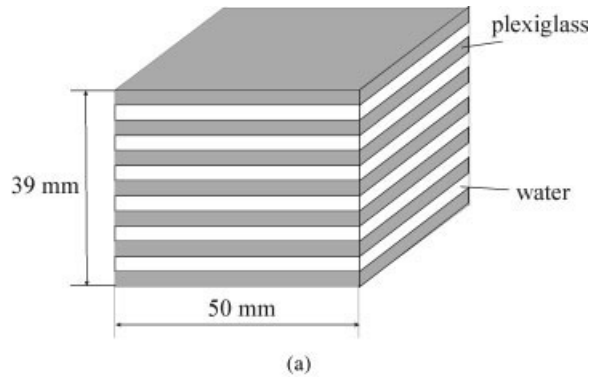


Figure 10 Picture and photographs of the phantom: (a) phantom schematics, (b and c) different views of phantom. Each water compartment is 3 mm thick.

coil was reproduced with minimal under- and overflows, as observed through an attached oscilloscope.

3. A spin-echo pulse sequence was selected with repetition time/echo time (TR/TE) = 2,000/20 ms. Here, the y -direction was used for frequency encoding. For transversal imaging, we

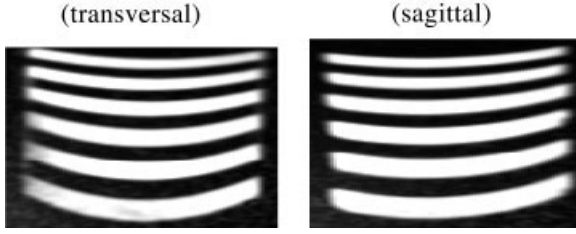


Figure 11 Resulting images obtained from a Plexiglas phantom with Cho's G_y surface coil (17). The coil plane resides 4.3 cm below the first water contour.

used the z -axis for slice selection and the x -axis for phase encoding. For longitudinal slices, the selection was changed as follows: the x -axis for slice selection and the z -axis for phase encoding.

Figure 11 depicts the images obtained from the phantom in the transversal and longitudinal plane. Image distortions are clearly observable, both in terms of undesirable curvature and nonuniform thickness layers. These results form the basis of improving the surface gradient coil designs. Specifically, by modifying the current flow patterns, it is hoped to maximize the magnetic field linearity.

THEORETICAL LEAST SQUARES FORMULATION

To significantly improve the existing surface gradient coil design, we devised a mathematical formulation that determines the optimal current distribution in a given coil plane based on a prescribed field linearity within a given ROI. The subsequent sections outline

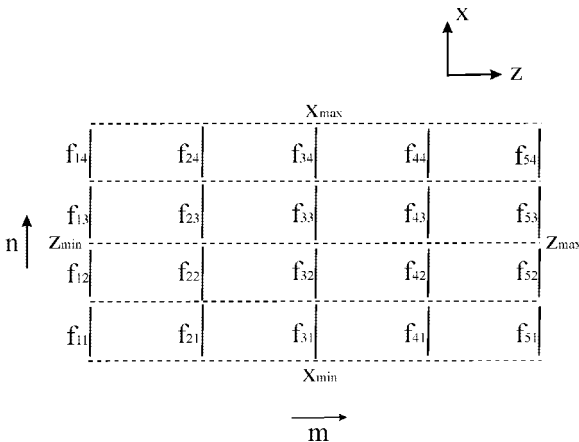


Figure 12 Set of basis function chosen for the proposed least squares method.

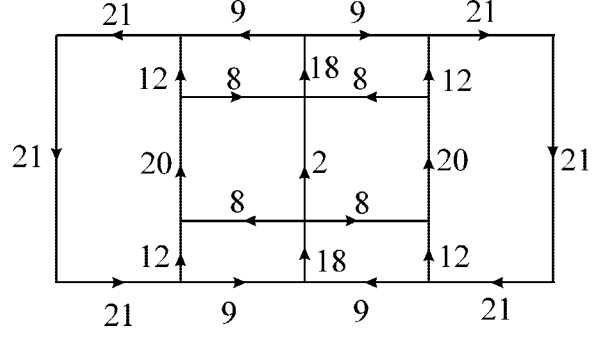


Figure 13 New 5×4 y -gradient coil design.

the necessary theoretical steps needed to arrive at an optimal current distribution.

We consider an excitation current density $\mathbf{j}(z, x)$ residing in the z - x -plane. Dictated by the bore size of the MR scanner, the uniplanar coil region is restricted to the following spatial dimensions:

$$\begin{aligned} & [z_{\min}, z_{\max}, x_{\min}, x_{\max}] \\ & = [-0.1, 0.1, -0.05, \text{ and } 0.05 \text{ m}]. \end{aligned}$$

Next, we consider a cubical ROI with the following spatial dimensions:

$$\begin{aligned} & [z_{\min}, z_{\max}, x_{\min}, x_{\max}, y_{\min}, y_{\max}] \\ & = [-0.025, 0.025, -0.025, 0.025, 0.04 \text{ and } 0.08 \text{ m}], \end{aligned}$$

which is sufficient in size to conduct cranial imaging of small animals such as rats and mice.

Now, our goal is to find the current density $\mathbf{j}(z, x)$ that yields a desired magnetic field distribution $B_{z,\text{des}}(z_o, x_o, y_o)$ inside the previously predefined ROI as depicted in Fig. 1. The starting point is the Biot-Savart integral law in the form

$$\mathbf{B}(\mathbf{r}_o) = \frac{\mu}{4\pi} \int \frac{\mathbf{j}' \times \mathbf{r}}{r^3} dS', \quad [1]$$

where $r = |\mathbf{r}_o - \mathbf{r}_s|$. Vector \mathbf{r}_o points to the coordinates of the observation point, residing inside the ROI, and \mathbf{r}_s refers to the coordinates of the unknown excitation source. Because we are interested in the z -component of the B field, we consider only the x -component of the surface current density $\mathbf{j}(z, x)$. Thus, Eq. [1] is rewritten as

$$B_z(\mathbf{r}_o) = \frac{\mu}{4\pi} \int \frac{\hat{\mathbf{x}} \times \mathbf{r}}{r^3} j_x(z, x) dS'$$

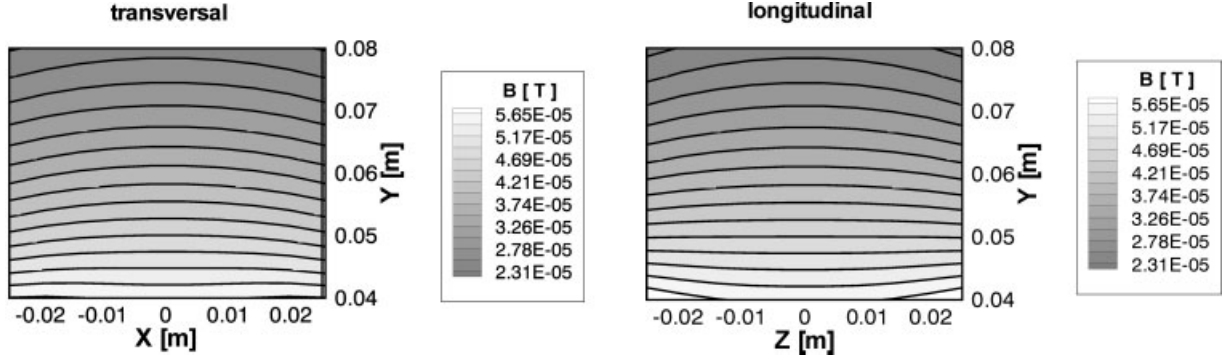


Figure 14 Magnetic field in teslas for the 5×4 y-gradient coil. All spatial dimensions are in meters.

$$= \frac{\mu}{4\pi} \int \frac{y_o}{|\mathbf{r}_o - \mathbf{r}_s|^3} j_x(z, x) dS_s, \quad [2]$$

where $\hat{\mathbf{x}}$ is a unit vector in x -direction. Explicitly, the flux density takes on the form

$$B_z(z_o, x_o, y_o) = \frac{\mu}{4\pi} \int_{x_{\min}}^{x_{\max}} \int_{z_{\min}}^{z_{\max}} \frac{y_o}{(y_o^2 + (x_o - x)^2 + (z_o - z)^2)^{3/2}} j_x(z, x) dz dx. \quad [3]$$

Because the sum of the inflowing coil current has to equal the sum of the exiting current, a constraint condition has to be imposed on $j_x(z, x)$, i.e.,

$$\int_{z_{\min}}^{z_{\max}} j_x(z, x) dz = 0, \quad [4]$$

for all values of x . Next, we approximate this x -directed current density $j_x(z, x)$ by a set of basis functions $f_n(z, x)$, $n = 1, \dots, N$ such that

$$j_x(z, x) = \sum_n^N I_n f_n(z, x). \quad [5]$$

Inserting Eq. [5] into Eq. [3] yields

$$B_z(z_o, x_o, y_o) = \frac{\mu}{4\pi} \sum_n^N I_n \int_{x_{\min}}^{x_{\max}} \int_{z_{\min}}^{z_{\max}} \frac{y_o f_n(z, x)}{(y_o^2 + (x_o - x)^2 + (z_o - z)^2)^{3/2}} dz dx. \quad [6]$$

Written in more compact notation, we write

$$B_z(z_o, x_o, y_o) = \sum_n^N I_n K_n(z_o, x_o, y_o), \quad [7]$$

where K_n is identified as

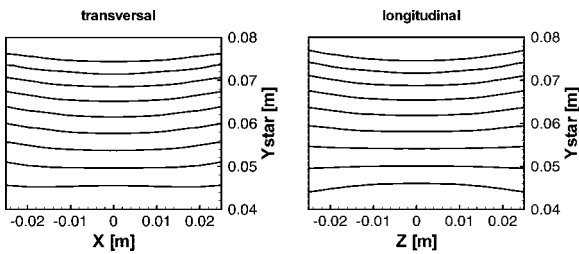


Figure 15 Simulations of the reconstructed image produced by the 5×4 y-gradient coil. All spatial dimensions are given in meters.

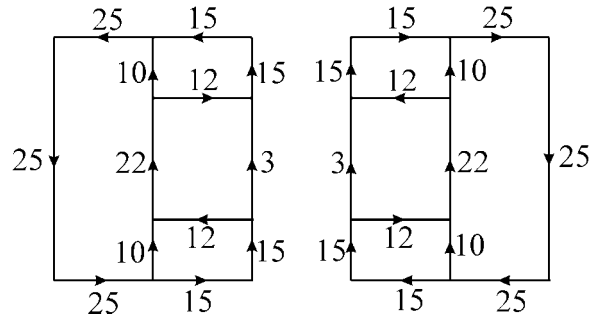


Figure 16 The 6×4 y-gradient coil.

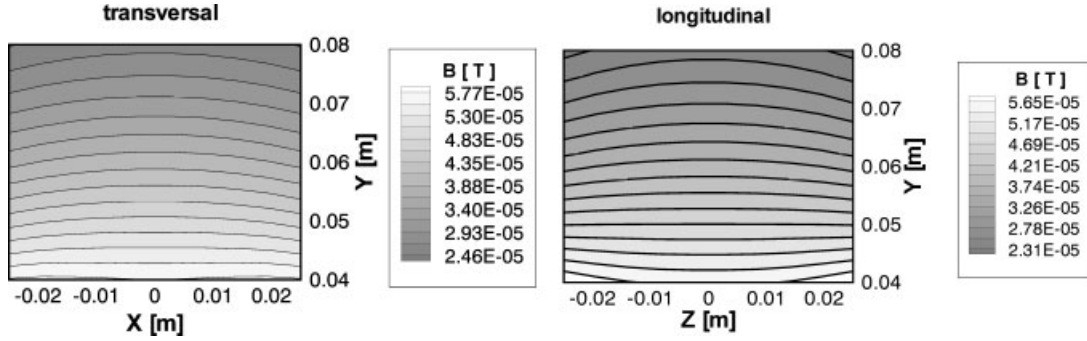


Figure 17 Magnetic field in teslas of the 6×4 y-gradient coil. All spatial dimensions are in meters.

$$K_n(z_o, x_o, y_o) = \frac{\mu}{4\pi} \int_{x_{\min}}^{x_{\max}} \int_{z_{\min}}^{z_{\max}} \frac{y_o f_n(z, x)}{(y_o^2 + (x_o - x)^2 + (z_o - z)^2)^{3/2}} dz dx. \quad [8]$$

As a next step, a functional Φ is established that relates the computed field B_z to the desired field $B_{z,\text{des}}$. In particular,

$$\Phi = \frac{1}{2} \iint_{\text{ROI}} W(z_o, x_o, y_o) \cdot [B_z(z_o, x_o, y_o) - B_{z,\text{des}}(z_o, x_o, y_o)]^2 dz_o dx_o dy_o + \int_{x_{\min}}^{x_{\max}} \lambda(x) \int_{z_{\min}}^{z_{\max}} j_x(z, x) dz dx. \quad [9]$$

Here, $W(z_o, x_o, y_o)$ is an arbitrarily chosen weight function. As discussed in the following paragraphs, by appropriately selecting this function, we can affect field linearity and homogeneity.

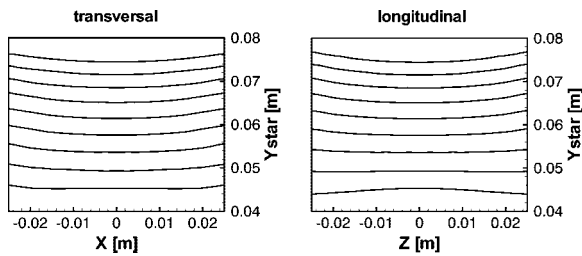


Figure 18 Simulations of the expected image reconstruction produced by the 6×4 y-gradient coil shown in Fig. 17. All spatial dimensions are in meters.

Our goal is to find $B_z(z_o, x_o, y_o)$, which minimizes the functional Φ . This is accomplished by setting the derivative of the functional to zero with respect to the unknown currents, i.e.,

$$0 = \frac{\partial \Phi}{\partial I_{n'}} = \iint_{\text{ROI}} W(z_o, x_o, y_o) \cdot \left[\sum_n I_n K_n(z_o, x_o, y_o) - B_{z,\text{des}}(z_o, x_o, y_o) \right] K_{n'}(z_o, x_o, y_o) dz_o dx_o dy_o + \int_{x_{\min}}^{x_{\max}} \lambda(x) \int_{z_{\min}}^{z_{\max}} f_{n'}(z, x) dz dx, \quad [10]$$

for $n' = 1, \dots, N$ and $0 = \partial \Phi / \partial \lambda$. The result can be cast as

$$0 = \sum_n I_n \int_{z_{\min}}^{z_{\max}} f_n(z, x) dz \quad \forall x. \quad [11]$$

From here, we obtain

Table 1 Gradient Strengths and Quality Factors of Three Monoplanar G_y Surface Gradient Coils

| Design | G_y [G/cm/100 A] (recorded at height $y = 6$ cm) | Q |
|----------------------------------------|----------------------------------------------------------|-------|
| Cho et al. [17] (maximum, 24 wires) | 15.50 | 0.867 |
| 5×4 y-gradient coil | 8.14 | 0.908 |
| 6×4 y-gradient coil | 8.26 | 0.915 |

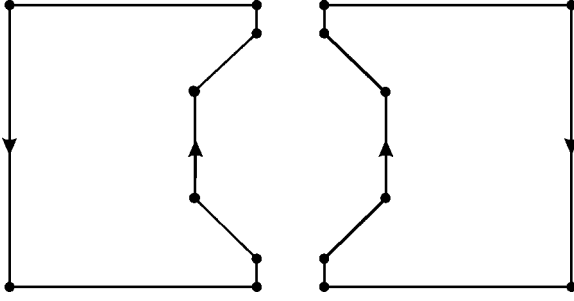


Figure 19 A y-gradient coil prototype.

$$\begin{aligned} \sum_n I_n \iiint_{\text{ROI}} W(z_o, x_o, y_o) K_n(z_o, x_o, y_o) \\ \times K_n'(z_o, x_o, y_o) dz_o dx_o dy_o = \iiint_{\text{ROI}} \\ \times W(z_o, x_o, y_o) K_n'(z_o, x_o, y_o) B_{z,\text{des}}(z_o, x_o, y_o) dz_o dx_o dy_o. \end{aligned} \quad [12]$$

As discussed further in detail, the left and right side of Eq. [10] can be cast as a system of linear equations in compact notation

$$\mathbf{AX} = \mathbf{b}. \quad [13]$$

Solving this system yields the vector \mathbf{X} that contains the discrete current elements I_n , $n = 1, \dots, N$, and λ .

We now consider a special choice of basis functions; specifically, functions f_{mn} are zero everywhere except that they behave like a δ -function, $\delta(z - z_m)$ over the interval $(z_m, x_n^-) - (z_m, x_n^+)$ (Fig. 12).

In this case, the function takes on the form

$$\begin{aligned} \Phi = \frac{1}{2} \iiint_{\text{ROI}} W(z_o, x_o, y_o) \cdot [B_z(z_o, x_o, y_o) \\ - B_{z,\text{des}}(z_o, x_o, y_o)]^2 dz_o dx_o dy_o \\ + \sum_n (\Delta x \lambda_n) \left(\sum_m I_{mn} \right). \end{aligned} \quad [14]$$

The last term follows from the limitation that is imposed on surface current.

$$\begin{aligned} K_{mn}(z_o, x_o, y_o) \\ = \frac{\mu}{4\pi} \int_{x_n^-}^{x_n^+} \frac{y_o}{(y_o^2 + (x_o - x)^2 + (z_o - z_m)^2)^{3/2}} dx. \end{aligned} \quad [15]$$

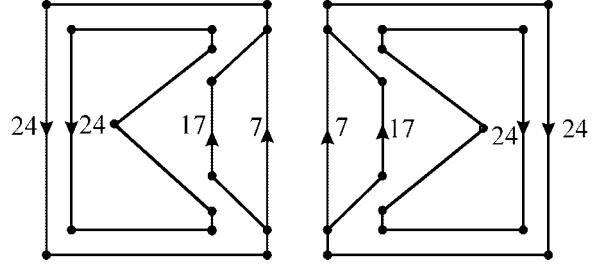


Figure 20 Six-loop coil y-gradient coil.

The resulting system of equations (Eq. [13]) has the following coefficients for matrix \mathbf{A} and column vector \mathbf{b} :

$$\begin{aligned} A_{M(n'-1)+m', M(n-1)+m} = \sum_{mn} \iiint_{\text{ROI}} W(z_o, x_o, y_o) \\ K_{mn}(z_o, x_o, y_o) K_{m'n'}(z_o, x_o, y_o) dz_o dx_o dy_o, \text{ for} \\ m, m' = 1, \dots, M \text{ and } n, n' = 1, \dots, N. \end{aligned} \quad [16]$$

$$\begin{aligned} A_{M(n'-1)+m', MN+n'} = 1, \text{ for} \\ m' = 1, \dots, M \text{ and } n' = 1, \dots, N. \end{aligned}$$

$$\begin{aligned} A_{MN+n', i} = 1, \text{ for } i = 1 + M(n' - 1), \dots, Mn' \\ \text{and } n' = 1, \dots, N. \end{aligned}$$

$$\begin{aligned} b_{M(n'-1)+m'} = \iiint_{\text{ROI}} W(z_o, x_o, y_o) \\ K_{m'n'}(z_o, x_o, y_o) B_{z,\text{des}}(z_o, x_o, y_o) dz_o dx_o dy_o, \text{ for} \\ m' = 1, \dots, M \text{ and } n' = 1, \dots, N. \end{aligned} \quad [17]$$

Furthermore, vector \mathbf{X} is comprised of the elements

$$\begin{aligned} X_{M(n'-1)+m'} = I_{m'n'}, \quad m' = 1, \dots, M, \\ n' = 1, \dots, N \end{aligned} \quad [18]$$

$$X_{MN+n'} = \Delta x \lambda_{n'}, \quad n' = 1, \dots, N. \quad [19]$$

Solving Eq. [13] either directly (via Gauss elimination) or iteratively (via conjugate gradient method) for the unknown currents I_{mn} yields the discrete current elements (magnitude and direction). After scaling these currents into integer values, we obtain the direction and discrete strength of each segment that should be placed into the grooves of the planar former. Typically, the discrete numbers should not

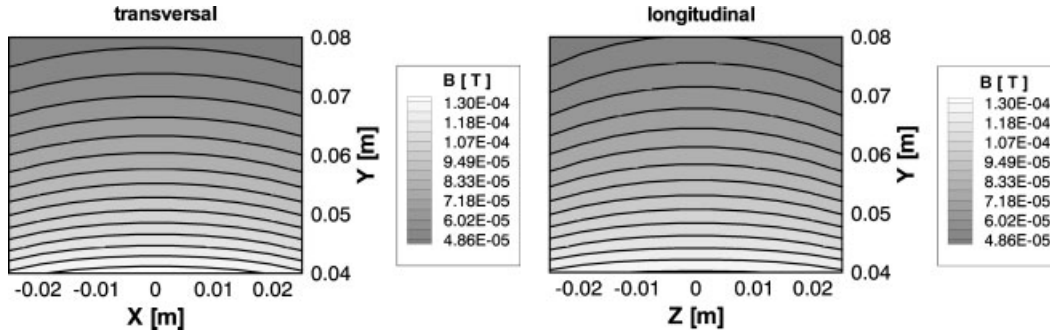


Figure 21 Magnetic field in teslas for the six-loop y -gradient coil. All spatial dimensions are recorded in meters.

exceed 24–25 in order to maintain appropriate compactness.

DEVELOPMENT OF THE Y -GRADIENT COILS USING THE LEAST SQUARES METHOD

In the following, the previously outlined mathematical design methodology is used to construct two novel surface gradient coil wire patterns with superior field strength and field uniformity. Although the approach is done for the construction of the G_y coil, a completely analogous approach is anticipated for the G_x and G_z surface coils.

G_y Gradient Coil with $m = 5$ and $n = 4$ (Labeled as 5×4 y -Gradient Coil)

The wire arrangement is depicted in Fig. 13. After solving Eq. [13] for the unknown currents, we arrive at the discrete current distributions within the generic layout pattern depicted in Fig. 12. The actual layout is displayed in Fig. 13. In this figure, the integers denote the number of wire segments carrying current in the indicated directions. The field produced by this coil is represented in Fig. 14. Theoretically, predicted image

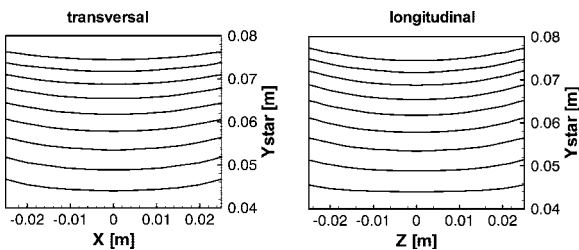


Figure 22 Simulations of the reconstructed image produced by the six-loop y -gradient coil. All dimensions are listed in meters.

distortions of the phantom placed with the coil's ROI are based on our earlier discussion (Fig. 5) and are shown in Fig. 15. We notice a compression of the upper layers (due to nonlinear flux distribution) and curvature (due to parasitic field distribution). In terms of the coil's figure of merit we obtain $Q = 0.908$, which represents a significant improvement over $Q = 0.867$, the baseline coil developed in Ref. (17).

G_y Gradient Coil with $m = 6$ and $n = 4$ (Labeled as 6×4 y -Gradient Coil)

As a second example, a configuration with $m = 6$, $n = 4$ is considered. Using the least squares method we obtain the wire distribution shown in Fig. 16. The corresponding field produced by this coil is represented in Fig. 17. Figure 18 provides the numerical predictions of the anticipated transversal and longitudinal (sagittal) distortions when a phantom is placed within the ROI.

Next, we will compare the strength of the surface gradient coils in the center of the ROI, as well as their respective quality factor for all three coils described previously. Table 1 reports the maximum field strength in the center of the ROI and the Q factor as defined previously. From Table 1, we notice that the 5×4 and 6×4 coils clearly yield better magnetic field uniformities. Consequently, the obtained images

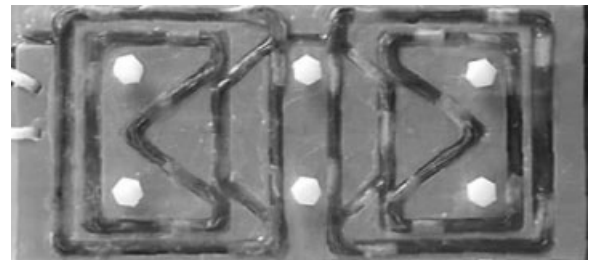


Figure 23 Six-loop y -gradient coil.

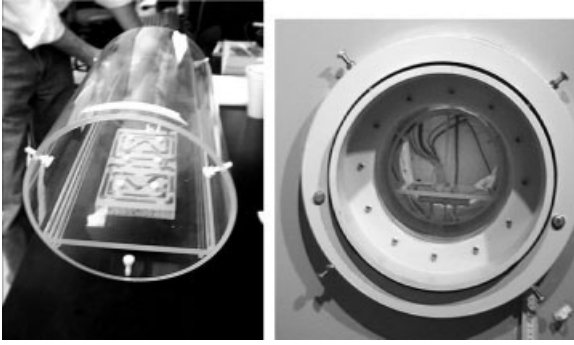


Figure 24 Photographs of the new G_y coil placed in a 25-cm diameter Plexiglas tubular cylinder (left) and placed inside the 4.7 T Bruker magnet with existing gradient set (right).

of the phantom are significantly less distorted. However, the gradient strengths produced by these coils are weaker than the one reported in Ref. (17). It is interesting to point out that these coil designs feature current elements that generally are farther away from the ROI. Consequently, the magnetic field can be made more uniform at the expense of field strength. However, the trade-off field strength vs field uniformity can be mitigated somewhat.

ADDITIONAL PERFORMANCE IMPROVEMENTS

There are certain design constraints that are difficult to overcome by using the least squares method. For instance, increasing the numbers m and n produce higher field uniformities at the expense of lowering the gradient strengths. Moreover, practical coil fabrication becomes increasingly difficult for coils with high numbers of m and n . Consequently, it is desirable to develop an alternate more effective approach for the surface coil design.

Toward this end, we can impose several practical restrictions to avoid making the design excessively cumbersome. Specific items include

1. The coil should be simple to build.
2. The number of wires in each groove should not exceed a value of 24–25.
3. The current-carrying wires (grooves) should not intersect.
4. The neighboring grooves should not be closer than 1 cm from each other.
5. The sharp angles at the coil nodes should be avoided.

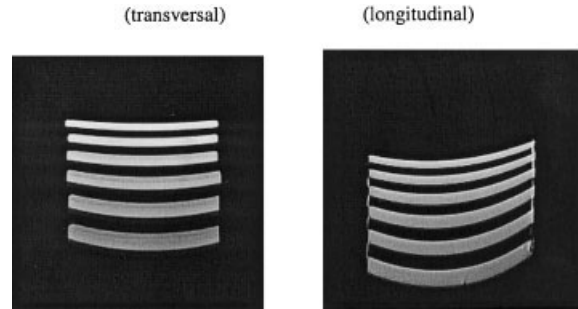


Figure 25 Resulting image of the phantom with the coil shown in Fig. 24.

Obviously, these conditions are difficult, if not impossible, to implement in terms of a simple least squares design method. However, the results obtained by this method along with previous designs can provide us with a hint as to how to place the wires in order to achieve a better gradient field. Our first goal is to consider a template as shown in Fig. 19.

This design considers two loops, each carrying 24 wires. We immediately notice a significant amount of unused space inside each loop. By placing additional wire configurations inside these loops, we are able to (i) improve the field strength and (ii) have more freedom to improve the field quality factor (i.e., lower the parasitic gradients). The nodal coordinates are optimized by trial and error, resulting in a design depicted in Fig. 20. We did not use any numerical optimization technique because it would be impossible to comply with all the restrictions listed previously. The corresponding magnetic field simulations produced by this G_y coil are depicted in Fig. 21. Examining the predicted distortions for a phantom placed within the ROI is shown in Fig. 22 for both the transversal and the sagittal (longitudinal) directions.

This coil yields an acceptable quality factor of $Q = 0.882$. The coil is constructed on a plastic former, seen in Fig. 23. Specifically, the G_y coil was wound on a planar 11×22 -cm Garolite (G-10) former with machined grooves. To preshape the wire pattern, enamel-coated copper wire of AWG-20 size was wound on a template before placing the pattern into the grooved former. An epoxy resin was used to fix the wire pattern within the former. We measured an inductance of $L_s = 0.496$ mH and a resistance of $R_s = 1.1 \Omega$, respectively.

This coil design was tested in a 4.7-T Bruker MR scanner with a 45-cm bore, shown in Fig. 24, with the resulting images from a phantom depicted in Fig. 25. There is an important reason why the lower portion of the longitudinal (sagittal) image in Fig. 25 appears distorted: it is difficult to measure precisely the distance

Table 2 Gradient Strength and Quality Factor of Six-Loop G_y Surface Gradient Coil

| Design | G_y [G/cm/100 A] (recorded at height $y = 6$ cm) | Q |
|---------------------------------------------------|----------------------------------------------------------|-------|
| Six-loop y -gradient coil (maximum 24 wires) | 20.80 | 0.880 |

between the coil plane and the lower edge of the phantom. The entire phantom in the experiment should have been positioned slightly closer to the coil than it was actually placed. The superior performance parameters of the 6-loop y -gradient coil both in terms of Q and in field strength are summarized in Table 2. Finally, Fig. 26 compares the various coil designs to the Cho design (17) by displaying the strength of the magnetic field along the vertical axis passing through the center of the ROI:

A set of preliminary experiments with a marmoset brain was performed in an effort to assess the image quality of a commercial encircling G_y coil (30.5-cm inner diameter Magnex gradient set of 68 mT/m; 220- μ s rise time) vs our novel six-loop planar G_y coil. For the direct comparison, the six-loop coil was used without shim currents and only minimal preemphasis current to obtain the same rise time. The applied drive current for the six-loop coil was adjusted to a maximum of 20 A, although currents of 100 A can be achieved. Basic testing in the MR scanner confirmed the fact that shimming of the six-loop coil is not needed.

The following MR parameters are used for the image acquisition: spin-echo pulse sequence, TR/

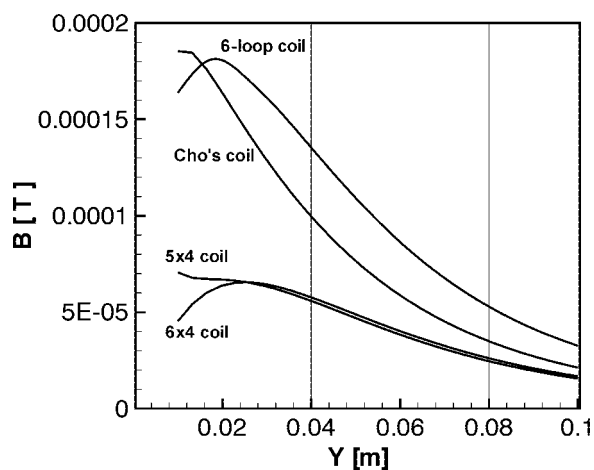


Figure 26 B_z component of the magnetic flux density in tesla's along the vertical line ($x = 0$ and $z = 0$) passing through the ROI: Cho's design (17), 5×4 design, 6×4 design, and six-loop design. Spatial dimension is recorded in meters.

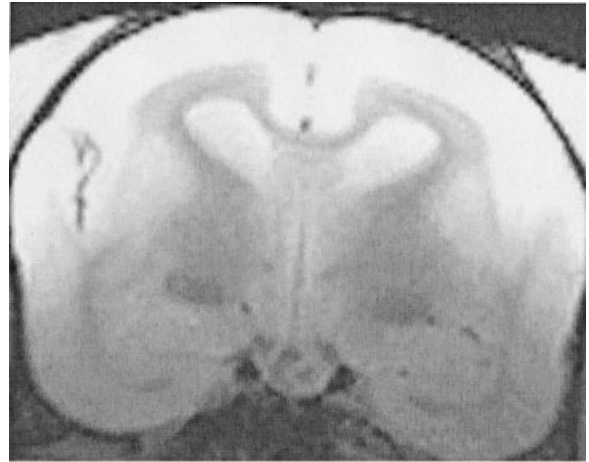
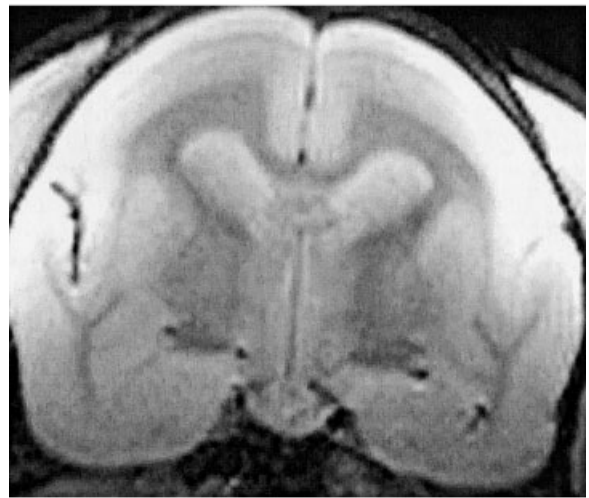
Bruker G_y gradient coil6-loop G_y gradient coil.

Figure 27 Resulting image of a marmoset brain acquired by a commercial gradient coil (top) and new G_y coil (bottom) depicted in Fig. 23. The surface coils were operated as phase-encoding gradients.

TE = 500/30 ms, field of view = 60 mm, 256×256 matrix size, and slice thickness = 1.0 mm. Figure 27 shows the transversal view of the cranial area. The slight asymmetry in the image observed with the six-loop coil is most likely because of the fact that the distance from coil plane to center of the ROI was larger than the targeted 6 cm.

CONCLUSIONS

This study proposed a new, systematic approach of designing monoplanar surface gradient coils by a

modified least squares solution of Biot-Savart's integral equation. The desired field distribution yields segmented current elements in terms of magnitude and direction. The elements can be arranged into individual loops and, subsequently, can be combined to create novel surface wire patterns.

Following our theoretical model predictions, a G_y gradient coil was constructed and the resulting field distributions were confirmed with a magnetic field sensor (Hall element). These measurements clearly show that not only can a strong gradient be generated, but the gradient field achieves a remarkable uniformity throughout the ROI.

Based on preliminary experiments we can conclude that the six-loop G_y surface gradient coil approach offers a simple and inexpensive construction that can be integrated easily into existing commercial MR scanners without major modifications. The attainable field strength and linearity show promise in providing high-resolution images from a localized ROI. The results of this research effort are encouraging in terms of designing and constructing the remaining G_x and G_z surface coils in a similar manner.

ACKNOWLEDGMENT

This work was supported by a grant from the National Institute of Mental Health, Translational Research and Scientific Technology Office, R41 MH064970.

REFERENCES

- Vaughan JT, Garwood M, Collins CM, Lui W, Delabarre L, Adriany G, Andersen P, Merkle H, Goebel R, Smith MB, Ugurbil K. 2001. 7 T vs. 4 T:RF power, homogeneity, and signal-to-noise comparison in head images. *Magn Reson Med* 46:24–30.
- Dubowitz DJ, Tyszka JM, Sewry CA, Moats RA, Scadeng M, Dubowitz, V. 2000. High-resolution magnetic resonance imaging of the brain in the *dy/dy* mouse with merosin-deficient congenital muscular dystrophy. *Neuromuscul Disord* 10:292–298.
- Hayes CE, Edelstein WA, Schenck JF, Mueller OM, Eash M. 1985. An efficient highly homogeneous radiofrequency coil for whole-body NMR imaging at 1.5T. *J Magn Reson* 63:622–628.
- Vaughan JT, Hetherington HP, Out JO, Pan JW, Prohast JM. 1994. High frequency volume coils for clinical NMR imaging and spectroscopy. *Magn Reson Med* 32:206–218.
- Bogdanov G, Ludwig R. 2002. Coupled microstrip line transverse electromagnetic resonator model for high-field magnetic resonance imaging. *Magn Reson Med* 47:579–593.
- Fisher T, Bogdanov G, Ludwig R, Silva AC, Merkle H, Ferris C. 2003. An RF microstrip resonator for imaging at 11.7 T. In: *Proceedings of the International Society for Magnetic Resonance in Medicine*, Toronto, ON, Canada.
- Shi F, Latour LL, Ludwig R, Sotak CH. 1996. A new design for a three-channel surface gradient coil employing a 3-D finite element model. *Magn Reson Med* 35:596–605.
- Steigerwald RL, Wirth WF. 2000. High-power, high-performance switching amplifier for driving magnetic resonance imaging gradient coils. In: *IEEE 31st Annual Power Electronics Specialists Conference Vol. 2*, pp 643–648.
- Liu H, Truwit CL. 1998. True energy-minimal and finite-size biplanar gradient coil design for MRI. *IEEE Trans Med Imaging* 17:826–830.
- Ersahin A, Hinks RS, Bronskill MJ, Henkelman RM. 1996. Biplanar gradient coil for interventional open-concept superconducting magnet. In: *Proceedings of the International Society for Magnetic Resonance in Medicine* p 124.
- Schweikert KH, Krieg R, Noack F. 1988. A high field air-cored magnet coil design for fast field-cycled NMR. *J Magn Reson* 78:77–96.
- Wong E, Jesmanowicz A, Hyde JS. 1991. Coil optimization for MRI by conjugate gradient descent. *Magn Reson Med* 21:39–48.
- Turner, R. 1988. Minimum inductance coils. *J Phys E Sci Instrum* 21:948–952.
- Compton RC. 1982. Gradient coil apparatus for a magnetic resonance system. U.S. Patent No. 4456881. Filed January 18, 1982; granted June 26, 1984.
- Green D, Bowtell RW, Morris PG. 2002. Uniplanar gradient coils for brain imaging. In: *Proceedings of the International Society for Magnetic Resonance in Medicine*, Honolulu, HI (in press).
- Shi F, Ludwig R. 1996. 2D and 3D numerical analysis of gradient and parasitic gradient fields of a three-channel surface gradient coil for magnetic resonance imaging. *IEEE Trans Magn* 32:195–207.
- Cho ZH, Yi JH. 1991. A novel type of surface gradient coil. *J Magn Reson* 94:471–485.
- Shi F, Ludwig R. 1998. Magnetic resonance imaging gradient coil design by combining optimization techniques with the finite element method. *IEEE Trans Magn* 34:671–683.